PROCEEDINGS A

royalsocietypublishing.org/journal/rspa

Research

**Cite this article:** Li K, Salmanidou D, Gopinathan D, Heidarzadeh M, Guillas S. 2025 Uncertainty in Manning's roughness coefficient in multilevel simulations of future tsunamis in Sumatra. *Proc. R. Soc. A* **481**: 20240637.
https://doi.org/10.1098/rspa.2024.0637

Received: 22 August 2024
Accepted: 1 May 2025

**Subject Areas:**
computer modelling and simulation, geophysics, statistics

**Keywords:**
hazard assessment, friction, multifidelity, probabilistic numerics, uncertainty quantification, coastal engineering

**Author for correspondence:**
Serge Guillas
e-mail: s.guillas@ucl.ac.uk

# Uncertainty in Manning's roughness coefficient in multilevel simulations of future tsunamis in Sumatra

Kaiyu Li[1], Dimitra Salmanidou[2], Devaraj Gopinathan[2], Mohammad Heidarzadeh[3] and Serge Guillas[1,2]

[1]Department of Statistical Science, and [2]Advanced Research Computing Centre, University College London, London WC1E 6BT, UK
[3]Department of Architecture and Civil Engineering, University of Bath, Bath BA2 7AY, UK

SG, 0000-0002-3910-3408

We employ multilevel Bayesian quadrature (MLBQ) to quantify uncertainties in the land cover roughness, a critical but unknown parameter for simulation of structural forces from future tsunamis that inform coastal engineering and urban planning. To account for this uncertainty, we regard roughness as a nuisance parameter and integrate out its effects on the maximum momentum flux. A comprehensive integration over a range of roughness requires large numbers of computationally expensive simulations. We circumvent this hurdle using multilevels of resolution for the simulations, a mix of two levels of mesh sizing for underlying non-uniform unstructured mesh—a low (50 m) and high (25 m) resolution. The computational burden of the overall integration is further reduced by blending the outputs of the multilevel simulations using Bayesian quadrature. Using end-to-end physical and numerical modelling to simulate the entire tsunami life-cycle—earthquake source to coastal inundation—we illustrate our approach by computing probability distributions of local

THE ROYAL SOCIETY
PUBLISHING

effects from future large tsunamis for Sumatra. Our MLBQ framework, accounting for uncertainties in roughness while reducing computational burden, can improve probabilistic hazard and risk assessments in combination with other uncertainties.

## 1. Introduction

As one of the most destructive natural disasters, tsunamis have caused a large number of casualties and economic losses in history. The long wavelengths of tsunami waves enable them to travel across large areas of the world's oceans and cause widespread destruction and death. The 2004 Indian Ocean tsunami generated by the M9.1 Sumatra–Andaman earthquake was the deadliest tsunami on record. The massive tsunami claimed the lives of more than 220 000 people and destroyed countless buildings and towns in countries surrounding the Indian Ocean, including Indonesia, Thailand, Sri Lanka and India among other countries, causing billions of dollars of economic loss [1]. More recently, the 2011 Tohoku tsunami pounded the northeastern coast of Japan, killing more than 19 000 people and left thousands missing. The tsunami also caused the Fukushima nuclear accident and the radiation leak, which brought extensive and severe negative effects [2,3].

Coastal engineering plays an important role in disaster mitigation. Constructing coastal barriers such as dikes, berms and embankments, and strengthening the seismic capacity of buildings can mitigate the effect and encroachment of tsunami waves and reduce the collapse and damage to buildings. For example, the results of the 2004 Indian Ocean tsunami field survey showed that port facilities such as breakwaters and sturdy coastal houses mitigated the damage due to the tsunami [4].

Studying future tsunami wave force acting on land structures is necessary for coastal engineering. Many studies mainly focus only on inundation depth [5]. The velocity of waves is also important in coastal engineering, e.g. when modelling tsunami empirical fragility [6]. The fluid force can be evaluated with hydrodynamic force, which is proportional to the momentum fluxes, a function of the inundation depth and the velocity of the flow. This is a more valid measure of forces on buildings than flow height or velocity. The quantity is essential for engineers when designing buildings with appropriate structural systems and materials to resist tsunami waves. For example, the quantity is used in Tohoku tsunami-induced building failure analysis [7]. By combining the results with the momentum fluxes of future tsunamis, engineers can have a better understanding of tsunami risks, leading to more effective coastal engineering in mitigating disasters.

One key ingredient in modelling tsunami flow is friction parametrization. Manning's $n$ parameter is a common choice due to its ease of understanding and low computational load. It is widely used in tsunami models [8] and recently other parametrizations have been proposed to improve the Manning coefficient with three parameters performing slightly better [9]. Manning's roughness coefficient $n$ is not directly measurable. The coefficient varies spatially based on roughness and other surface characteristics of the seabed. However, calibration of $n$ values for tsunami modelling remains limited [8,10,11]. Many tsunami modellers rely on standard values from the literature, despite the fact that $n$ is varied and uncertain. This approach potentially underestimates the mitigation effects of forests and structures [8]. Active research has been conducted to constrain the roughness coefficient [12,13]. Sensitivity analyses have shown that the epistemic uncertainty in Manning's roughness coefficient significantly affects the simulation results [11,14,15], including velocity, inundation and momentum flux, which we demonstrate later in this study.

Our goal in this paper is to quantify the epistemic uncertainty arising from a lack of knowledge of the Manning coefficient values, using the methodology of multilevel Bayesian probabilistic numerical methods built with Gaussian processes (GPs) to enable efficient computations. Our assumptions are that expert knowledge can provide a distribution of the unknown Manning

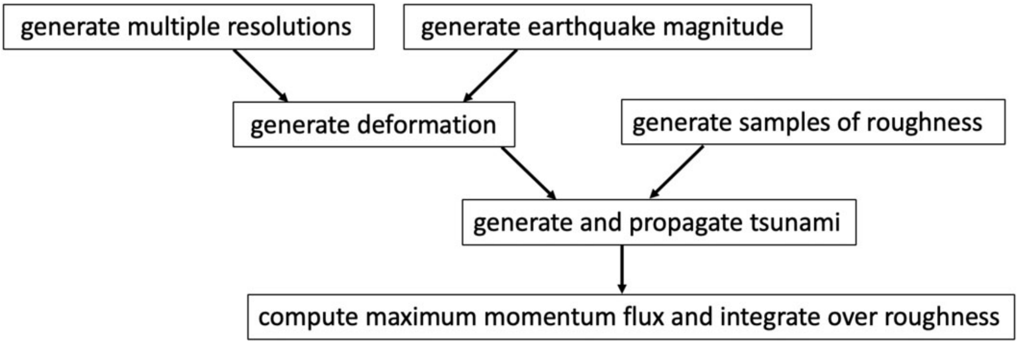

**Figure 1.** Flowchart illustrating the integration of various components employed in this study.

coefficients (albeit here with two examples), and that the friction is uniform everywhere on land for the purpose of illustration. The overall implication of our approach is that one needs to think about the level of uncertainty in the nature of the friction over the landscape as it can yield large variations, especially when the friction levels are deemed to be smaller—possibly wrongly as often.

In the following sections of the paper, we employ Volna-OP2[1] as the tsunami simulator [16,17] to simulate the complete life cycle of a tsunami, capturing wave velocity and inundation depths for up to 3 h post-earthquake. This simulator is efficient and robust, having been successfully used in the past [18–20]. When simulating with Volna-OP2, the roughness coefficient remains constant in time and space, as in many tsunami models. Given the epistemic uncertainty of the roughness coefficient and its significant effect on momentum flux, we treat it as a nuisance parameter. To address this, we employ a novel Bayesian probabilistic numerical method, specifically, multilevel Bayesian quadrature (MLBQ) [21], to perform the integration. It is possible to account for other sources of uncertainties in probabilistic hazard and risk assessments, such as in the study by Fukutani *et al.* [22] that considered the uncertainty of random tsunami sources and seawall height, but here we focus on Manning's roughness coefficient.

Figure 1 presents a flowchart illustrating the integration of various components used throughout this study. In the subsequent sections of the paper we explain these components in detail. In §2 we describe tsunami simulation methods. In §3 we demonstrate the effect of Manning's roughness coefficient. In §4, we assume a Beta distribution on the roughness parameter and use MLBQ that combines low- and high-resolution tsunami modelling to efficiently estimate the integrated maximum momentum flux of Sumatra tsunamis.[2] It is possible to include more levels, as in [21,23,24]; however, we use two levels here for simplicity. We use five values at coarse resolution and three values at fine resolution to cover the space of $n$ optimally in terms of computational burden. By doing so, we propagate uncertainties from the roughness coefficient to the maximum momentum flux (the maximum over time).

## 2. Tsunami simulation

In this section, we describe the numerical simulation models for the generation, propagation and inundation of tsunami waves. In subsequent sections, we use these simulations to estimate the integrated maximum momentum flux, a measure of tsunami intensity, at 12 selected gauge locations. These gauges, illustrated in figure 2, are situated near the port of Meulaboh, a coastal city in the neighbourhood of the Sumatra subduction zone. The Sumatra subduction zone is an

---

[1] v 1.5 available at https://github.com/reguly/volna and https://zenodo.org/records/1413124, with upgraded second-order finite-volume scheme and boundary conditions.

[2] The code and data for this implementation are available at https://github.com/CeciliaKaiyu/UQfriction and https://doi.org/10.5281/zenodo.15015626.

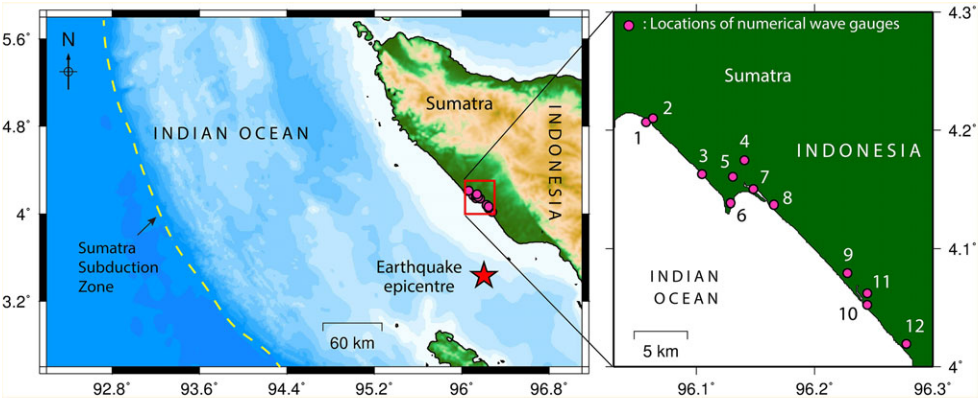

**Figure 2.** Geographical locations of 12 gauges and the earthquake epicentre.

area of frequent seismic activity due to its location on the Pacific Ring of Fire [25]. For each gauge, we analysed two synthetic megathrust scenarios in the Indian Ocean, as shown in figure 3.

## (a) Earthquake source

We use a finite-fault segmentation model along with the Okada equations [26] to generate the seabed deformation (uplift and subsidence) due to the earthquake in the Sumatra subduction zone. The earthquake epicentre is positioned at (3.4332°N, 96.2018°E), close to the epicentre of 2004 Sumatra–Andaman earthquake (3.3°N, 96.0°E), where the 2004 mainshock rupture began [27]. Lay *et al.* [27] display a dense concentration of earthquake occurrences within our region of interest (figure 2), showing a substantial number of seismic events. Given the occurrence of the two most significant earthquakes within the past 40 years in this subduction zone, i.e. the events on 26 December 2004 (Mw 9.1) and 28 March 2005 (Mw 8.6), we select two earthquakes of magnitudes 8.7 and 9.2, respectively, in our study.

The finite fault encompasses the region of interest selected from the Sumatra subduction zone (figure 3). The Slab2 model is restricted to depths ranging from 7 km to 100 km and limited geographically between 6.5644°N and 9.3210°S, and 92.5139°E and 106.8591°E. Within this region, the finite-fault segmentation approximates a curved rectangle with corners: southwest (9.3210°S, 106.4920°E), southeast (6.6296°S, 106.8591°E), northeast (6.5644°N, 94.7940°E) and northeast (5.8120°N, 92.5139°E). We discretize the fault into 20 × 203 (along-dip × along-strike) nearly rectangular segments as it is a common practice in earthquake and tsunami research (e.g. [28]). Each segment is on average 11 km (along-dip) ×15 km (along-strike) in area.

Okada's closed-form equations are used to compute the static vertical displacement $u_z$ at each segment. These finite-fault parameters *viz.*, depth, strike, dip angle, are sourced from Slab2 [29] (figure 3). The rake is assumed to be 90°. Slip profiles are constructed for the two events using compact positive kernels, as in Gopinathan *et al.* [19]. The resulting displacement profiles are used as initial conditions to generate the tsunami in Volna-OP2.

## (b) Tsunami propagation

Volna-OP2 [17] is an efficient tsunami simulator which simulates the complete life cycle of a tsunami from generation, propagation and inundation on shore. It uses a finite-volume discretization to solve the depth-averaged nonlinear shallow water equations in two horizontal dimensions

$$\left.\begin{aligned} &\frac{\partial H}{\partial t} + \nabla \cdot (H\mathbf{v}) = 0 \\ \text{and}\qquad &\frac{\partial H\mathbf{v}}{\partial t} + \nabla \cdot \left(H\mathbf{v} \otimes \mathbf{v} + \frac{g}{2}H^2\boldsymbol{I}\right) = -gH\nabla h, \end{aligned}\right\} \tag{2.1}$$

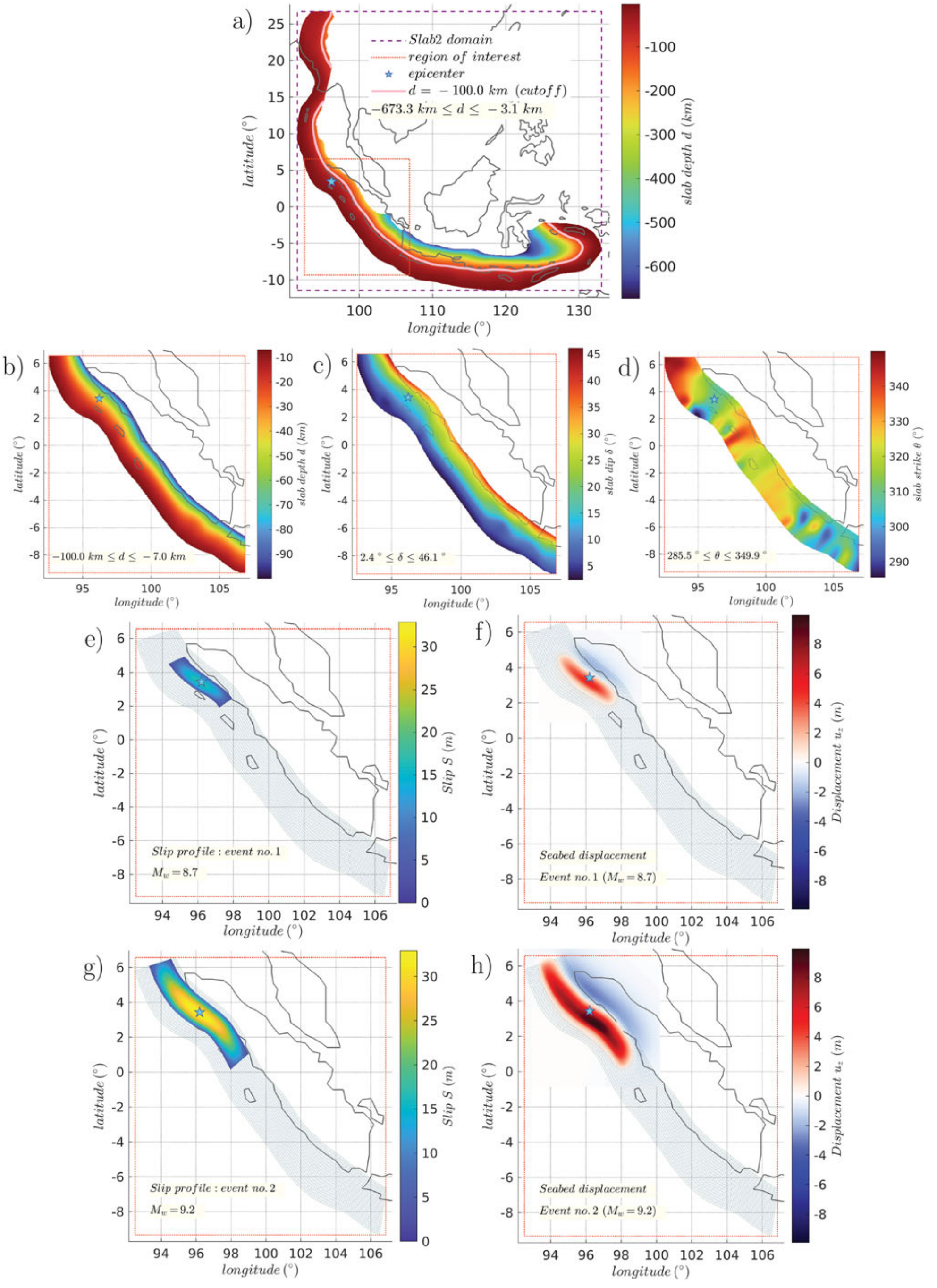

**Figure 3.** Slab2 geometry and fault model. The subduction geometry of Sumatra–Java subduction zone is taken from Slab2 (a) with the region of interest around Sumatra. A cutoff depth (100 km) is used to constrain the Slab2 data *viz.*, subduction depth (b), dip angle (c), and strike angle (d) which are used to inform the finite-fault segmentation. The slips for the two sources (e,g) give rise to the deformations (f,h).

where the total water depth $H$ is the sum of the dynamic bathymetry $h$ and the free-surface elevation $\eta$. The dynamic bathymetry is the sum of static bathymetry and the seabed deformation. The static bathymetry/topography is composed from GEBCO 2022 [30], Batimetri Nasional (BATNAS) bathymetry at 6″ (approx. 180 m), and Digital Elevation Model Nasional (DEMNAS) topography at 0.27" (approx. 8 m).[3] Here $g$ denotes the acceleration due to gravity, $\mathbf{v}$ is the fluid velocity in two horizontal directions and $\boldsymbol{I}$ denotes a $2 \times 2$ identity matrix. Using an unstructured triangular mesh with Volna-OP2, we are able to resolve complex bathymetry and topography, including coastlines up to the mesh resolution.

We use two meshes, a coarse and a fine mesh for the simulation, as shown in figure 4 denoting the low- and high-resolution simulations in our multilevel framework. The OceanMesh package [31] is used to generate the unstructured triangular mesh, which is finely resolved near the few main coastline cites including Meulaboh, and more coarse elsewhere (figure 4a). The simulations using Volna-OP2 are executed on a single NVIDIA P100 GPU (the Wilkes2 machine at Cambridge's CSD3). The simulations with a fine mesh require approximately 430 s per run, while those with a coarse mesh take less than 25 s.

These simulations can be used to estimate potential damage to buildings from future tsunamis and thus help mitigate the disaster. In coastal engineering, such estimates are useful for designing tsunami-resistant structures and determining optimal locations for counter-tsunami barriers to protect important buildings and human lives. As mentioned earlier, the hydrodynamic forces of tsunamis on structures in the inundation zone are proportional to the momentum flux [32]. Therefore, momentum flux is used to estimate hydrodynamic force in recent studies and has been suggested to be of use as an intensity measure for tsunami fragilities [33,34]. To quantify this, we define the momentum flux $M(t)$ as

$$M(t) = \rho ||\mathbf{v}(t)||_2^2 \, d(t),$$

where $\mathbf{v}$ is velocity, $d$ is the inundated depth and $\rho$ is fluid density. We assume $\rho$ to be $1\,\mathrm{kg\ m^{-3}}$ throughout. In our experiments, we simulate the propagation of tsunamis for 3 h following an earthquake and take the maximum momentum flux $M^{\max}$ over this period as our intensity measure:

$$M^{\max} = \max_{0<t\leq 10\,800\,s} M(t).$$

The output (tsunami wave height and speed) from the tsunami simulator is a time series. This means that the output is generated and recorded over time, capturing the changes in wave height and speed at various points in time. The maximum momentum flux with a specific roughness coefficient is obtained from tsunami simulations, along with time series output of inundation depth and velocity. There is a small time step in the outputs. For the fine mesh, this time step is approximately 0.217 s, while for the coarse mesh, it is approximately 0.416 s.

## 3. The effect of Manning's roughness coefficient

To assess the sensitivities of numerical simulations to Manning's roughness coefficient's $n$, we use the Volna-OP2 code to simulate tsunamis for each earthquake source using different $n$ values. In our simulations, Manning's roughness coefficient operates by attenuating tsunami momentum when the bathymetric depth exceeds the −50 m threshold. Figures 5 and 6 show the inundation depths and velocities at two chosen gauges, gauge 4 and gauge 10, simulated with three different Manning's roughness coefficients $n$, 0.01, 0.03 and 0.05. Figure 5 corresponds to the 8.7 magnitude earthquake, while figure 6 corresponds to the 9.2 magnitude earthquake. These figures show that Manning's roughness coefficient $n$ has a significant effect on tsunami behaviour, with inundation depths and velocities varying considerably across different $n$ values. For the magnitude 8.7 earthquake (figure 5), when the $n$ value is low (0.01 or 0.03), both gauges are inundated. At $n = 0.05$, only gauge 10 experiences inundation. When the earthquake magnitude is 9.2, both gauges are inundated even at higher $n$ values.

There are also differences between the momentum fluxes simulated at different resolutions. The effect of grid size is not as important as the dependence on Manning's coefficient. Figure 7 shows the momentum flux obtained at gauge 4 and gauge 10 under both high- and low-resolution

---

[3] both BATNAS and DEMNAS data are available from https://tanahair.indonesia.go.id/portal-web/unduh.

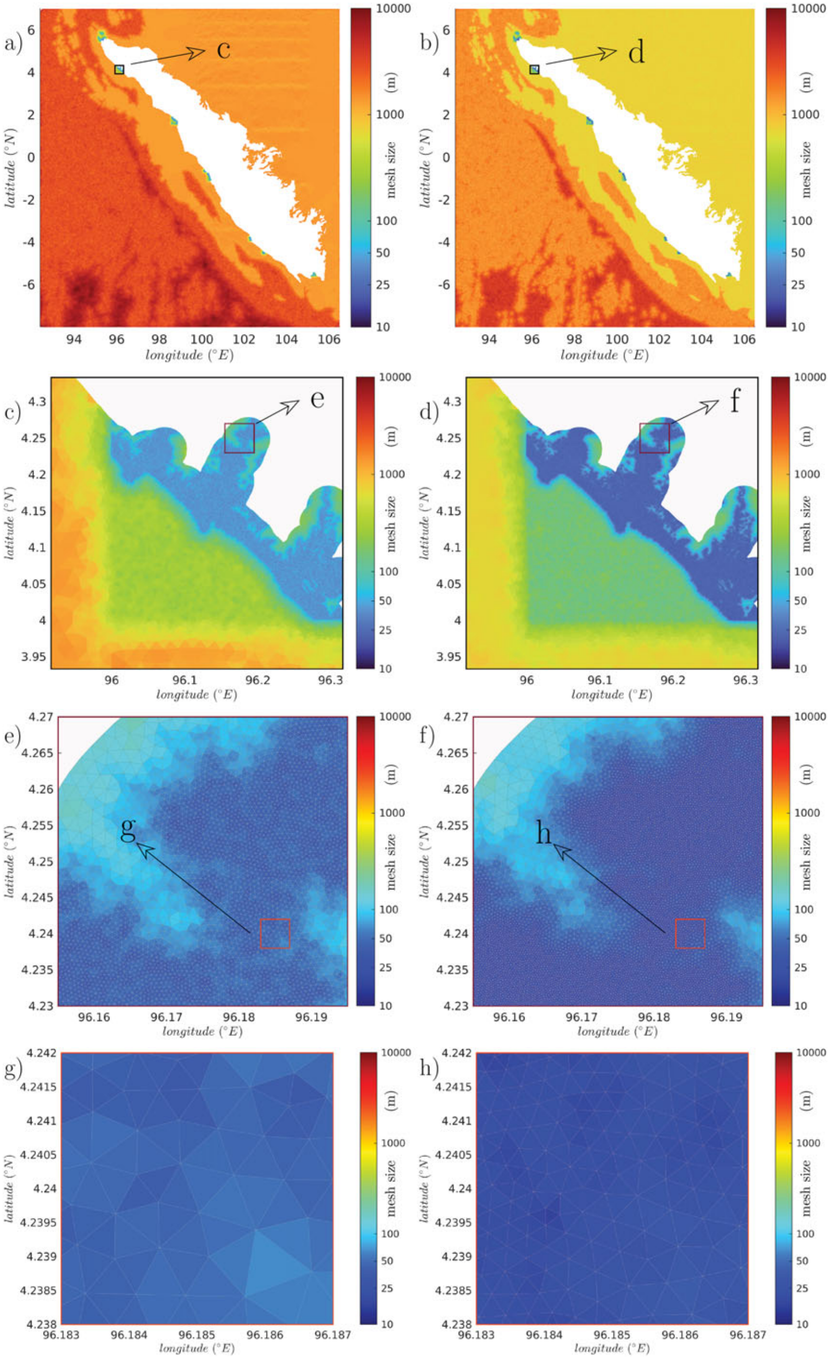

**Figure 4.** Coarse (a,c,e,g) and fine (b,d,f,h) mesh sizes of a small area near Meulaelboh Port used in low- and high-resolution simulations. The boxes in the meshes are magnified to show the difference in mesh sizes up to coastal resolutions of 50 m (g) and 25 m (h). Mesh (or triangle) sizes are shown in metres on the colour bar.

levels for magnitude of 8.7 or 9.2. The roughness coefficient is 0.03. Note that, the momentum flux scales obtained at gauge 4 and gauge 10 differ significantly; however, both plots indicate that the low-resolution level tends to underestimate the momentum flux and fails to accurately capture the peak.

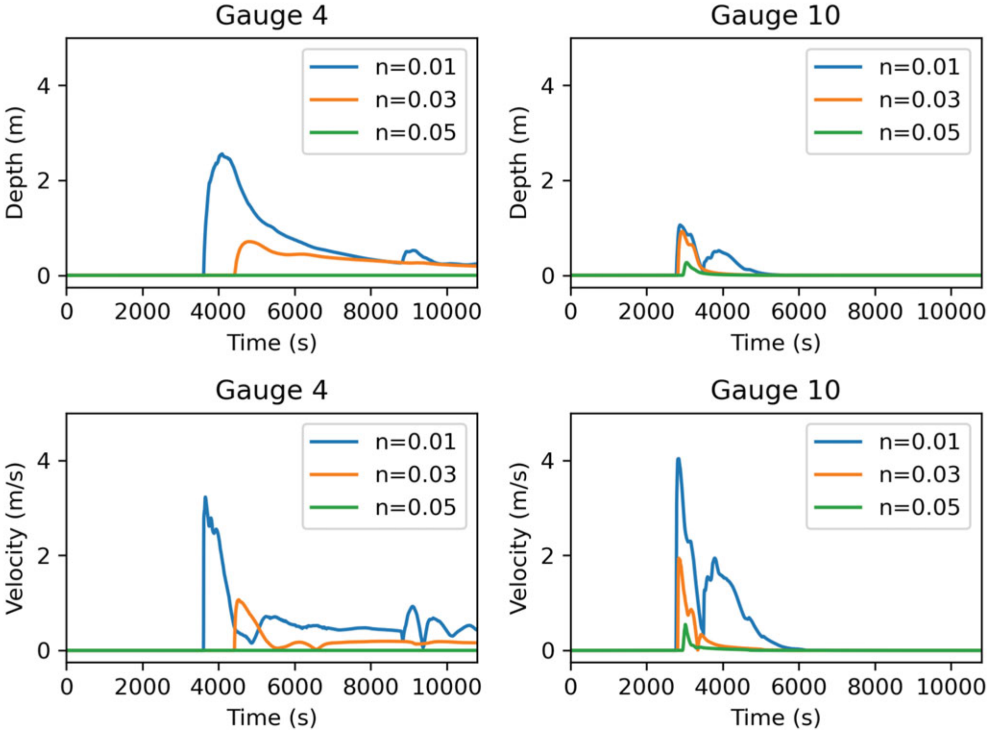

**Figure 5.** Sensitivity to Manning's roughness coefficient *n* for inundation depth and velocity at gauge 4 and gauge 10 with $n = 0.01$ (blue), $n = 0.03$ (orange) and $n = 0.05$ (green) when the earthquake magnitude is 8.7.

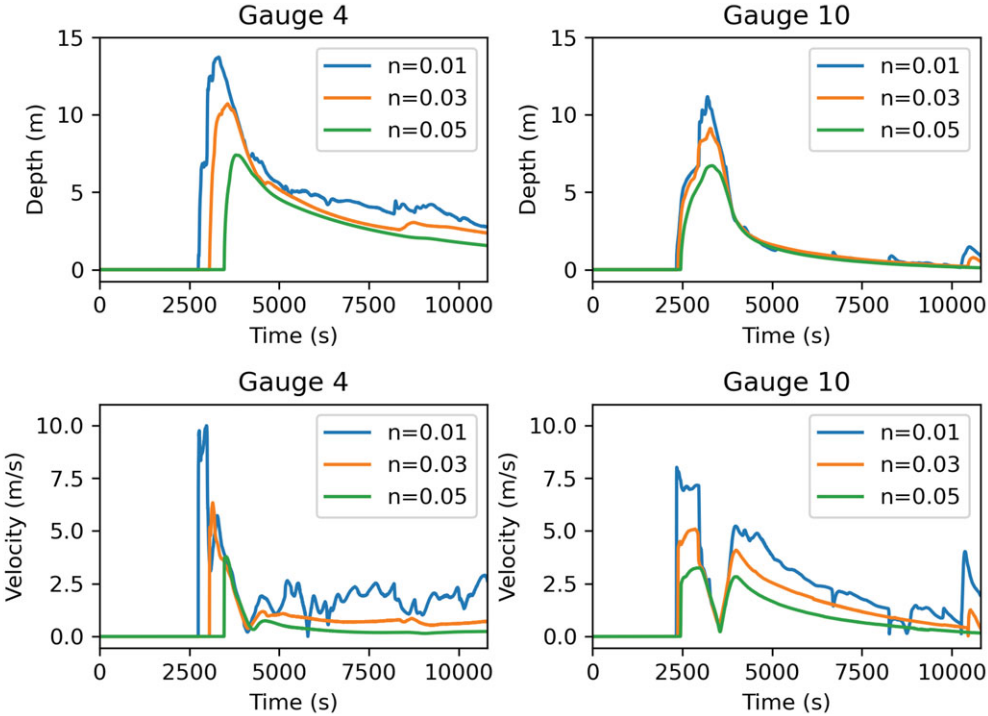

**Figure 6.** Sensitivity to Manning's roughness coefficient *n* for inundation depth and velocity at gauge 4 and gauge 10 with $n = 0.01$ (blue), $n = 0.03$ (orange) and $n = 0.05$ (green) when the earthquake magnitude is 9.2.

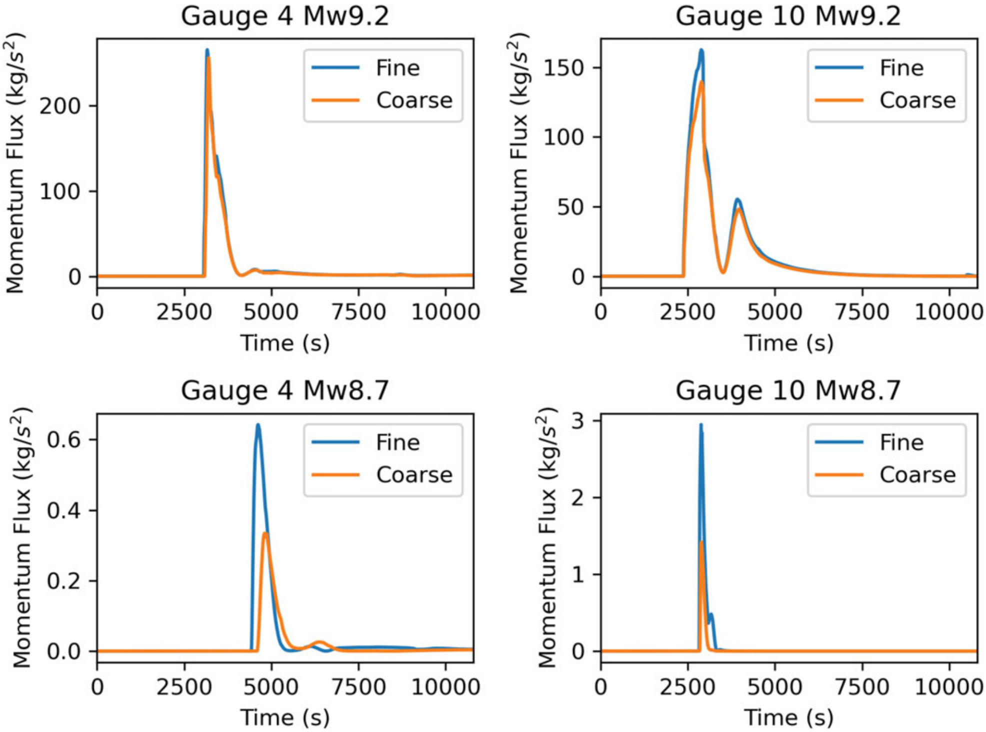

**Figure 7.** Momentum flux obtained at gauge 4 and gauge 10 under high- (blue) and low- (orange) resolution level for magnitudes of 8.7 or 9.2.

## 4. Integrated maximum momentum flux

CITE KOTANI and also other calibration [12] in the section/Should we change the section title?

Based on our simulation results from the previous section, tsunami simulations are sensitive to Manning's roughness coefficient. This emphasizes the need to quantify the epistemic uncertainty of $n$ in tsunami hazard and risk assessments. Rather than using fixed values, Bayesian methods model the epistemic uncertainty as probability distributions over parameters. Therefore, we deal with the uncertainty by assigning $n$ a probability distribution $q(n)$ and integrating over this nuisance parameter: $\int M^{\max}(n)q(n)\,\mathrm{d}n$, where $M^{\max}(n)$ is our quantity of interest (maximum momentum flux) computed using the value of $n$ in the simulation. This integration averages the maximum momentum flux for all possible values of $n$ and weights according to their probabilities. This is the integration we use to tackle the uncertainty. This approach reduces reliance on a single fixed $n$.

To model the uncertainty in Manning's roughness coefficient, we assign a Beta distribution to $n$ within the range $[0.01, 0.09]$. Some others have proposed up to 0.12 [35] for an upper range but it would only be applicable to a local coefficient representing a settlement not a constant coefficient for the whole area in our case. We reparametrize $n$ using the following transformation:

$$x = \frac{n - 0.01}{0.09 - 0.01}.$$

This transformation maps $n \in [0.01, 0.09]$ to $x \in [0, 1]$. Then, we can compute the integration over the interval $[0, 1]$, which aligns with the domain of the Beta distribution. The Beta distribution is an appropriate choice for this parameter as it is naturally constrained to a bounded interval and provides more flexibility than a uniform distribution. It allows us to incorporate expert knowledge by shaping the distribution and assigning higher probabilities to more likely values. We consider two Beta distributions with $n$ centred around 0.026 and 0.05: Beta(2, 5) and Beta(3, 3),

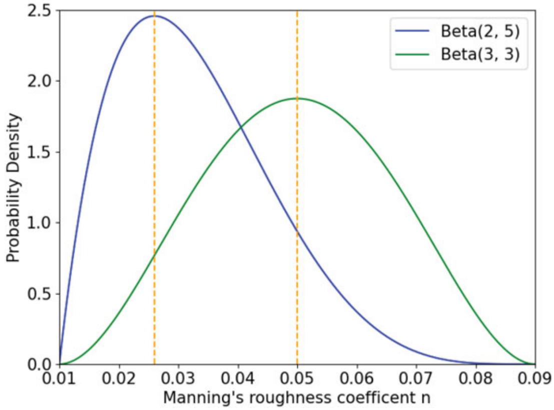

**Figure 8.** Beta distribution plot.

to illustrate how a different expert knowledge of the local friction could lead to different results. We found that in this latter choice, the means and uncertainties are smaller, indicating how influential is this first expert elicitation.

The probability distribution of the reparametrized parameter $x$ is illustrated in figure 8. Given this reparametrization, the integration becomes

$$\int_{0.01}^{0.09} M^{\max}(n)q(n)\,\mathrm{d}n = \int_0^1 M^{\max}(x)p(x)\,\mathrm{d}x,$$

where $p(x)$ is the probability distribution of $x$.

For complex models such as our tsunami simulator Volna-OP2, MLBQ is particularly suitable to estimate this integration efficiently. We denote by $M_l^{\max}(x)$ the maximum momentum flux obtained from simulations employing Manning's roughness coefficient $n = 0.08x + 0.01$, with mesh resolutions categorized into levels: $l \in \{0, 1\}$. Here, level 0 represents the lower-resolution level, while level 1 corresponds to the higher-resolution level. Given the multiple levels, the integration we are estimating is at the high-resolution level: $\int_0^1 M_1^{\max}(x)p(x)\,\mathrm{d}x$. MLBQ expresses the integral as the telescoping sum below:

$$\int_0^1 M_1^{\max}(x)p(x)\,\mathrm{d}x = \int_0^1 (M_1^{\max}(x) - M_0^{\max}(x))p(x)\,\mathrm{d}x + \int_0^1 M_0^{\max}(x)p(x)\,\mathrm{d}x, \tag{4.1}$$

and estimates each integral in the telescoping sum using Bayesian quadrature [36–38]. Low-resolution runs are employed to reduce the computational burden as multilevel methods do (see Li *et al.* [21] for instance showing many illustrations and theories). Intuitively, $(M_1^{\max} - M_0^{\max})$ tends to have lower variance, and within a multilevel framework, we can estimate the related integral accurately using a few points. Since $M_0^{\max}$ has lower simulation costs and higher variance, we can use more points to estimate the related integral accurately. Indeed running high-resolution simulations only could become prohibitive (though not in our case, which is designed to illustrate the benefits, but in more realistic hazard assessments).

Note that, the MLBQ estimator does not impose restrictions on point selection. Therefore, we opt for a uniform grid when selecting input points. At high- and low-resolution level, we use a uniform grid to draw quasi-uniform points $X_1 = (x_{(1,1)}, \ldots, x_{(1,3)})^\top$ and $X_0 = (x_{(0,1)}, \ldots, x_{(0,5)})^\top$, respectively. These point sets are mutually exclusive. We show all points in figure 10. Users can change the proportion of points across levels, but higher levels are costlier and usually have smaller variance. Thus, we use fewer points at high-resolution level. The number of points and the location of these points will affect the result. Some comparisons have been made in the paper by Li *et al.* [21]. We compute $M_0^{\max}(x_{(0,i)})$ for $x_{(0,i)}$, where $i \in \{1, \ldots, 5\}$. In addition, for each $x_{(1,i)}$ we compute $M_0^{\max}(x_{(1,i)})$ and $M_1^{\max}(x_{(1,i)})$, for $i \in \{1, 2, 3\}$.

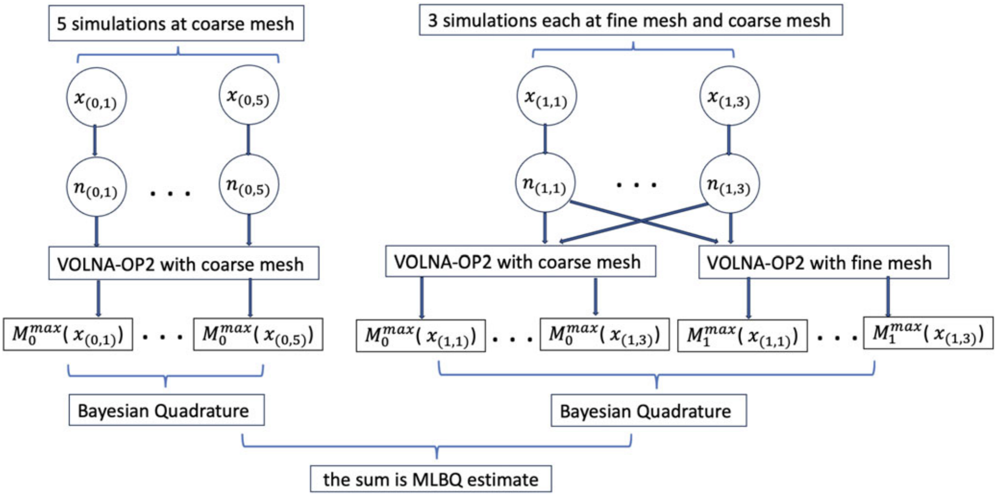

**Figure 9.** Flowchart illustrating the process of tsunami simulations using Volna-OP2 for implementing MLBQ. This procedure is executed simultaneously for all gauges.

Figure 9 illustrates how the tsunami simulations using Volna-OP2 are designed to implement MLBQ. First, the quasi-uniform points $X_0$ and $X_1$ are mapped to their corresponding Manning's roughness coefficients: $\{n_{(0,1)}, n_{(0,2)}, \ldots, n_{(0,5)}\}$ for $X_0$ and $\{n_{(1,1)}, n_{(1,2)}, n_{(1,3)}\}$ for $X_1$. Then, Volna-OP2 is run with a coarse mesh for each roughness coefficient $\{n_{(0,1)}, n_{(0,2)}, \ldots, n_{(0,5)}\}$, followed by simulations using both coarse and fine meshes for each roughness coefficient in $\{n_{(1,1)}, n_{(1,2)}, n_{(1,3)}\}$. In total, eight runs with coarse mesh and three runs with fine mesh are conducted. The maximum momentum flux is computed for each simulation. These results are then used to estimate the MLBQ.

As we mentioned, MLBQ estimates each integral in the telescoping sum (equation (4.1)) using Bayesian quadrature [36–38]. The MLBQ method initially specifies GP priors, $\mathcal{GP}(m_1, c_1)$ and $\mathcal{GP}(m_0, c_0)$, on the integrands $M_1^{\max} - M_0^{\max}$ and $M_0^{\max}$, respectively. Subsequently, given the simulation results, it can obtain the GP posterior on each integrand. Figure 10 shows posterior GPs at each level of MLBQ. The plot also shows that GP at level 0 performs well on all testing data. As we observed, GP at level 1 has fewer training data but still performs well on most testing data. However, it is a common challenge for GP that the fitting is poor near the boundaries of the input space. In addition, given that the distribution is Beta, the boundary region has less effect on the results. The plot also shows that the magnitude of the integrand at level 1 is much smaller than the magnitude of the integrand at level 0. The small scale makes level 1 less effective in the overall integral calculation and may result in a relatively small percentage bias. In addition, the maximum momentum flux decreases rapidly at low roughness values and more slowly as roughness increases. Similar phenomena have been observed in other gauges.

The GP posterior on the integrands $M_1^{\max} - M_0^{\max}$ and $M_0^{\max}$ then implies a pushforward posterior on the corresponding integrals $\int_0^1 (M_1^{\max}(x) - M_0^{\max}(x)) p(x)\,\mathrm{d}x$ and $\int_0^1 M_0^{\max}(x) p(x)\,\mathrm{d}x$, which are of interest to us. The pushforward posterior distribution for each integral takes the form of a Gaussian distribution. The sum of the means of these posterior Gaussian distributions yields the mean of the posterior distribution for $\int_0^1 M_1^{\max}(x) p(x)\,\mathrm{d}x$ (equation (4.2)), which is also the MLBQ estimate:

$$\begin{aligned}(\Pi[m_0] + \Pi[c_0(\cdot, X_0)]c_0(X_0, X_0)^{-1} M_0^{\max}(X_0))\\ + (\Pi[m_1] + \Pi[c_1(\cdot, X_1)]c_1(X_1, X_1)^{-1}(M_1^{\max}(X_1) - M_0^{\max}(X_1))),\end{aligned} \tag{4.2}$$

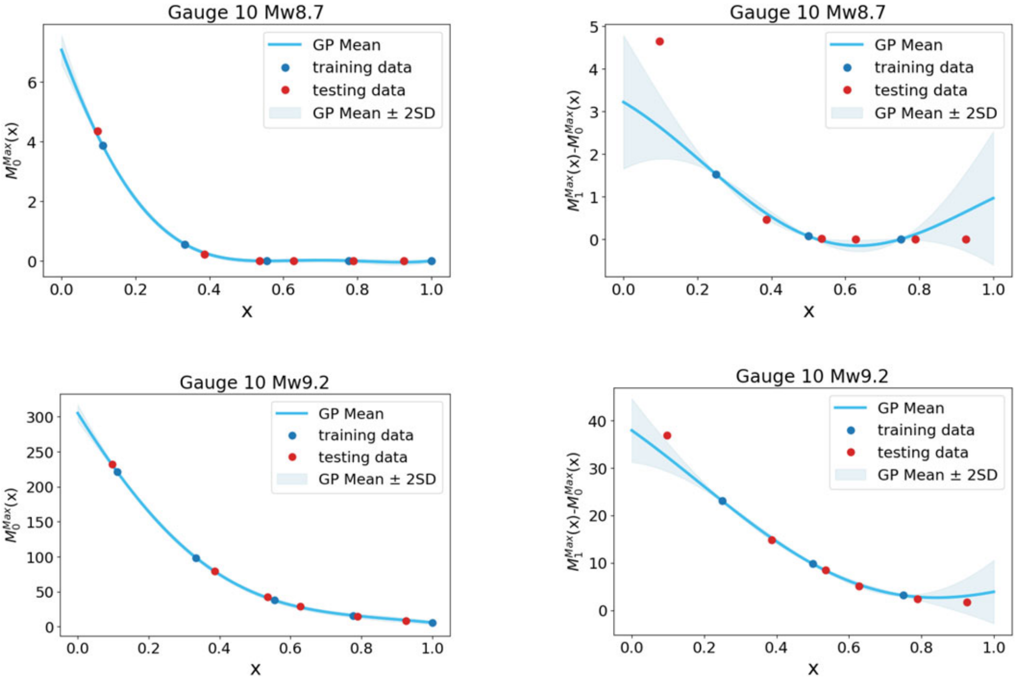

**Figure 10.** Gauge 10: Underlying GPs at level 0 ($M_0^{\max}$) (left) and at level 1 ($M_1^{\max} - M_0^{\max}$) (right) of MLBQ for the earthquake of magnitude 8.7 Mw and 9.2 Mw.

where $\Pi[c_l(\cdot, X_l)] = (\Pi[c_l(\cdot, x_{(l,1)})], \ldots, \Pi[c_l(\cdot, x_{(l,N_l)})])^\top$ is the kernel mean provided in appendix A, $(c_l(X_l, X_l))_{i,j} = c_l(x_{(l,i)}, x_{(l,j)})$ for all $i, j \in \{1, \ldots, N_l\}$, with $N_0 = 5$, $N_1 = 3$, and $M_k^{\max}(X_l) = (M_k^{\max}(x_{(l,1)}), \ldots, M_k^{\max}(x_{(l,N_l)}))^\top$ for all $(k, l) \in \{(0, 0), (1, 1), (0, 1)\}$.

We use this quantity in figure 11, where the integrated maximum momentum flux represents MLBQ estimates, accounting for the uncertainty of Manning's roughness coefficient. Manning's roughness coefficient values such as 0.025 and 0.03 are values commonly used in many applications [10,11,35]. Therefore, we compare simulation results with one fixed value of Manning's roughness coefficient (0.03 chosen as a typical choice in modelling and around the values we end up with, showing some larger and some smaller values than our approach at some gauges, demonstrating our point) and simulation results that take into account the uncertainty of Manning's roughness coefficient but integrates this uncertainty. The point estimate of momentum flux at various gauges from MLBQ accounts for the underlying uncertainty. The physical relationship is nonlinear, which affects the integrated value of the maximum momentum flux. Depending on location, this MLBQ point estimate may be higher or lower than a single maximum momentum flux computed by the simulator using a fixed Manning's roughness coefficient. The earthquake magnitude is 8.7. The figure illustrates that neglecting the uncertainty of roughness and relying on a fixed value could lead to potential overestimations or underestimations as observed in the Beta(2, 5) cases. Expert knowledge also has a significant effect on the integrated maximum momentum flux, with the Beta(3, 3) distribution resulting in much smaller values at all gauges compared with others.

The MLBQ estimator also provides the variance of the posterior Gaussian distribution on $\int_0^1 M_1^{\max}(x)p(x)\,\mathrm{d}x$:

$$
\begin{aligned}
&(\Pi[\Pi[c_0]] - \Pi[c_0(\cdot, X_0)]c_0(X_0, X_0)^{-1}\Pi[c_0(X_0, \cdot)]) \\
&\quad + (\Pi[\Pi[c_1]] - \Pi[c_1(\cdot, X_1)]c_1(X_1, X_1)^{-1}\Pi[c_1(X_1, \cdot)]),
\end{aligned}
$$

where $\Pi[\Pi[c_l]]$, $l \in \{0, 1\}$, is the initial error provided in appendix A.

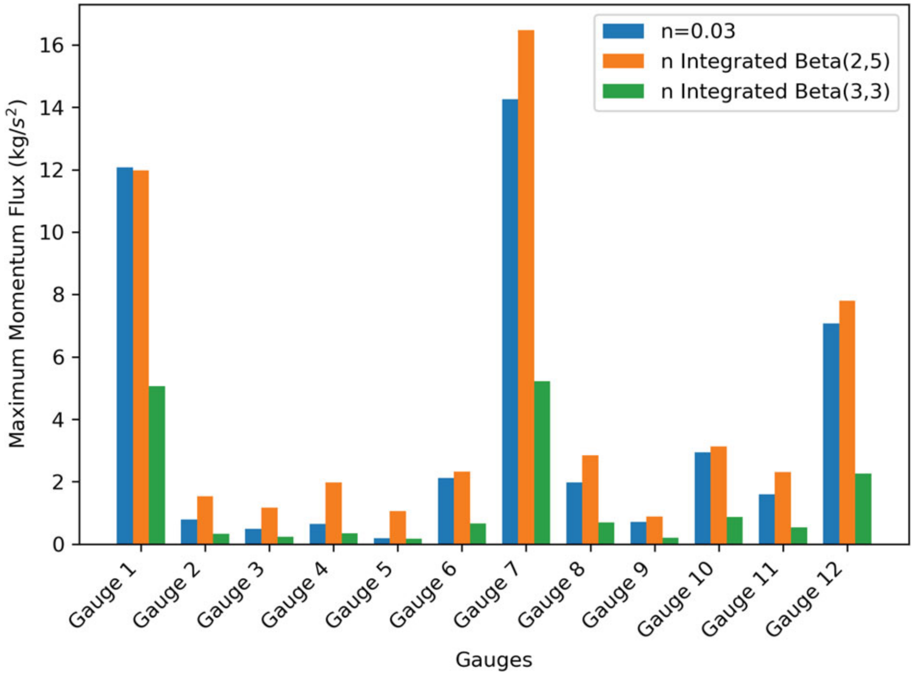

**Figure 11.** Comparison between the integrated maximum momentum flux from the MLBQ estimator and the maximum momentum flux with $n = 0.03$ at different gauges for an earthquake magnitude of 8.7.

Figure 12 shows the posterior distribution of the integrated maximum momentum flux at 12 gauges of tsunami caused by the 9.2 magnitude earthquake. These distributions are Gaussian distributions since they can be viewed as integrated GPs. Although it may not be a perfectly realistic modelling as negative values could be taken with some non-negligible probability, one can improve by using methods such as reparametrization if needed. We merge the two choices of Beta distributions for the Manning coefficient in figure 12 to demonstrate the effect of different assumptions. The notable difference between the two Gaussian distributions reflects the influence of different assumptions on the results. This illustrates that our method effectively propagates assumptions about the friction parameters into their effect on maximum momentum flux. The shapes and locations of the distributions in figure 12 reveal further effects of the values of Manning's coefficient on to the inundation. These distributions reflect the uncertainty associated with the estimated integrals. Indeed, a narrower distribution indicates that we have higher confidence in the MLBQ estimate, suggesting that the estimate is more stable. Conversely, a wider distribution represents higher uncertainty in the MLBQ estimate. To reduce the variance, possible strategies include further improving sampling strategy, increasing sample sizes, etc. It is not necessarily related to the amount of travel of the flow over land although the larger the mean value, the larger the variance about the mean in these simulated outputs of momentum flux. Overall, the behaviour of the flow with respect to Manning's coefficient at a specific location needs to be computed using our approach to reflect potential destructive nature of the flow.

The integrated maximum momentum fluxes can be further used for probabilistic tsunami hazard assessment and uncertainty analysis, including and not limited to building fragility curves construction or estimating probability of building damage. The results can be combined with building tsunami fragility curves (e.g. [39]) and be used to predict the probability of building with different materials getting damaged. For example, according to fig. 6 of [39] and figure 12 where the maximum momentum flux at gauge 7 is over 300 kg s$^{-2}$, the probability is high for reinforced concrete moment frame buildings with one to three stories subject to a 'complete' damage state (which means '100% economic loss, long-term building closure or more than partial or full

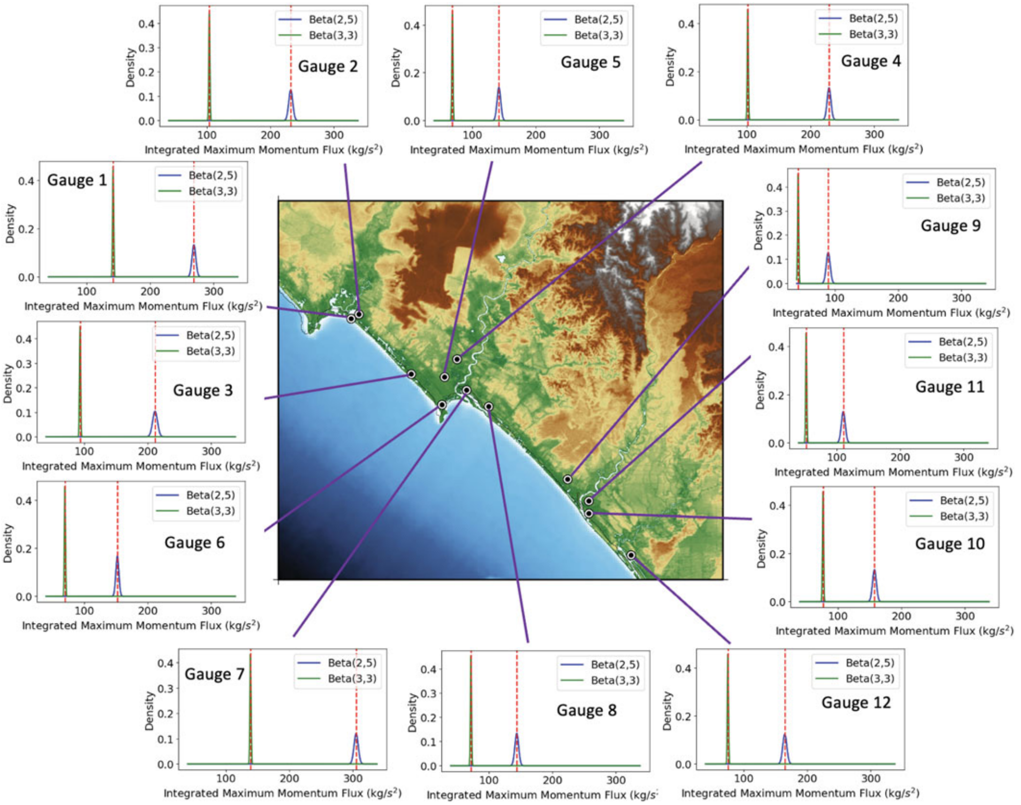

**Figure 12.** Posterior distribution of integrated maximum momentum flux at each gauge for an earthquake magnitude of 9.2. Dashed lines are the means (also known as the MLBQ estimates).

collapse, including washed away'). Note that the fragility curves for buildings are themselves probabilistic. To compute the risk for a building (or a set of buildings) being damaged, and at what level, one can use a catastrophe model, see [40] where tsunami hazard was combined with a probabilistic vulnerability function to obtain an end-to-end risk assessment, including even economic losses if values are known.

## 5. Conclusion

We compute the distribution of the maximum momentum flux at various locations, resulting from the approximation of the integration of the momentum flux over the distribution of possible values of Manning's roughness coefficient describing the land cover friction. We make use of Bayesian quadrature to achieve this computationally prohibitive integration over the set of uncertain values of the Manning's coefficient. This is a novel computation for tsunami modelling that we have made even more efficient by enabling two grid resolutions to be employed (one coarse, one refined) to reduce computational costs further. As a result, future tsunami hazard and risk assessments may employ these distributions to reflect more accurately the actual risk. Indeed, the land cover is often uncertain and changing in time due, e.g. to urban planning, agricultural practices or climate change; therefore, there is a need to reflect this uncertainty in risk assessments.

Bathymetry uncertainties are often large and can result in vastly different effects compared to the case when they are unaccounted for, see e.g. [41] for an illustration of the effect. To represent and propagate bathymetry uncertainties is a challenge, due to the high-dimensional complexity of the surface: see [42] for a solution using GP emulation and dimension reduction. The computation of the combined effect of bathymetry uncertainties with uncertainties in the friction modelling onshore is desirable in future tsunami hazard assessments.

In more complex modelling scenarios, the study area is segmented and classified, with each segment being assigned a corresponding Manning's roughness coefficient value [14,35]. In future applications using detailed roughness maps for tsunami inundation modelling, our approach could incorporate Manning's coefficient from various areas as a high-dimensional variable, thus enhancing flexibility. Our approach assumes that an expert can provide a reasonable estimate of Manning's roughness coefficient. However, this estimate is typically a spatially averaged value and may not fully capture local variations, especially in near-shore regions with distinct terrain characteristics. For hazard assessments, it is crucial to account for a range of realistic values, ideally informed by spatially varying land-use data. While a fixed uniform value may not be optimal, a uniform value with associated uncertainties is preferable to an incorrect fixed estimate.

The next steps include combining future probabilistic earthquake hazard with this integrated uncertainty in the Manning's coefficient to deliver fully representative hazard assessments. Merging these novel hazard footprints with uncertain vulnerability curves in a catastrophe model will produce probabilistic risk assessments as [15] illustrated the joint sensitivity for a small number of earthquake sources only and [22] demonstrated for a sea-wall not over land friction. Other future work includes representing not only the maximum momentum flux but the whole time series of momentum flux over the entire tsunami event to reflect scouring and other repetitive effects on buildings and structures. Ultimately, policy making and emergency planning will benefit from more such improvements in the precision of tsunami risk assessments, especially when combined with economic effects [40].

**Data accessibility.** The code and data for this implementation are available at [43] and [44].

**Declaration of AI use.** We have not used AI-assisted technologies in creating this article.

**Authors' contributions.** K.L.: conceptualization, data curation, formal analysis, investigation, methodology, software, validation, visualization, writing—original draft, writing—review and editing; D.S.: conceptualization, formal analysis, investigation, methodology, software, supervision, validation, visualization, writing—original draft; D.G.: data curation, investigation, resources, software, visualization, writing—original draft, writing—review and editing; M.H.: investigation, methodology, validation, visualization, writing—review and editing; S.G.: conceptualization, formal analysis, funding acquisition, methodology, project administration, supervision, validation, writing—original draft, writing—review and editing.

All authors gave final approval for publication and agreed to be held accountable for the work performed therein.

**Conflict of interest declaration.** The authors have no financial or proprietary interests in any material discussed in this article.

**Funding.** We acknowledge funding from the Lloyd's Tercentenary Research Foundation, the Lighthill Risk Network and the Lloyd's Register Foundation-Data Centric Engineering Programme of the Alan Turing Institute. S.G. was funded by EPSRC project EP/W007711/1 'Software Environment for Actionable & VVUQ-evaluated Exascale Applications' (SEAVEA). M.H. was partly funded by the Royal Society, the United Kingdom, grant number CHL/R1/180173. D.G. was supported by the EPSRC Impact Acceleration Account (IAA) award to UCL 2017-2022 (grant no. EP/R511638/1), and 2022-25 (grant no. EP/X525649/1).

**Acknowledgements.** This work was performed using resources provided by the Cambridge Service for Data Driven Discovery (CSD3) operated by the University of Cambridge Research Computing Service (www.csd3.cam.ac.uk), provided by Dell EMC and Intel using Tier-2 funding from the EPSRC (capital grant EP/T022159/1), and DiRAC funding from the Science and Technology Facilities Council (www.dirac.ac.uk). The authors would like to thank Jack Dignan for his help with the visualization of figure 12, and Daniel Giles for helpful discussions. Geospatial figures were created using The Generic Mapping Tools version 6 [45].

## Appendix A. Kernel mean and initial error

### (a) Beta distribution Beta(2, 5)

The probability density function (PDF) of the Beta distribution Beta$(2, 5)$ is given by

$$p(x; 2, 5) = \frac{x^{2-1} \cdot (1-x)^{5-1}}{B(2, 5)},$$

where $B(2,5)$ is the Beta function defined as $B(2,5)=\Gamma(2)\cdot\Gamma(5)/\Gamma(2+5)$. When $c$ is a squared exponential kernel with length-scale $\gamma$, the kernel mean can be computed analytically as

$$\begin{aligned}
\Pi[c(\cdot,x)] &= \int_0^1 \exp\left(-\frac{(x-x')^2}{\gamma^2}\right)\frac{x'(1-x')^4}{B(2,5)}\,\mathrm{d}x' = (15\gamma/4)\\
&\quad\times\left\{-2\exp\left(-\frac{(-1+x)^2}{\gamma^2}\right)\gamma(4\gamma^4+2(-1+x)^3x+\gamma^2(4-13x+9x^2))\right.\\
&\quad+2\exp\left(-\frac{x^2}{\gamma^2}\right)\gamma(4\gamma^4+2(-1+x)^4+\gamma^2(12+x(-20+9x)))\\
&\quad+\sqrt{\pi}(4(-1+x)^4x+3\gamma^4(-4+5x)+4\gamma^2(-1+x)^2(-2+5x))\\
&\qquad\left.\left(\operatorname{erf}\left(\frac{1-x}{\gamma}\right)+\operatorname{erf}\left(\frac{x}{\gamma}\right)\right)\right\},
\end{aligned}$$

and the initial error can be computed analytically as

$$\begin{aligned}
\Pi\Pi[c(\cdot,\cdot)] &= \int_0^1\int_0^1 \exp\left(-\frac{(x-x')^2}{\gamma^2}\right)\frac{x(1-x)^4}{B(2,5)}\frac{x'(1-x')^4}{B(2,5)}\,\mathrm{d}x'\,\mathrm{d}x\\
&= \frac{5}{77}\exp\left(-\frac{1}{\gamma^2}\right)\gamma^2\\
&\quad\times\left(28+3\exp\left(\frac{1}{\gamma^2}\right)\gamma^2(385+4\gamma^2(77-44\gamma^4+50\gamma^6))\right.\\
&\quad\left.-2\gamma^2(117+2\gamma^2(190+3\gamma^2(-19+6\gamma^2+50\gamma^4)))\right)\\
&\quad-\frac{5}{77}\gamma(-28+11\gamma^2(20+81\gamma^2))\sqrt{\pi}\operatorname{erf}\left(\frac{1}{\gamma}\right).
\end{aligned}$$

## (b) Beta distribution Beta(3, 3)

The PDF of the Beta distribution Beta$(3,3)$ is given by

$$p(x;3,3)=\frac{x^{3-1}\cdot(1-x)^{3-1}}{B(3,3)},$$

where $B(3,3)$ is the Beta function defined as $B(3,3)=\Gamma(3)\cdot\Gamma(3)/\Gamma(3+3)$. When $c$ is a squared exponential kernel with length-scale $\gamma$, the kernel mean can be computed analytically as

$$\begin{aligned}
\Pi[c(\cdot,x)] &= \int_0^1 \exp\left(-\frac{(x-x')^2}{\gamma^2}\right)\frac{x'^2(1-x')^2}{B(3,3)}\mathrm{d}x'\\
&= \frac{15}{4}\gamma\left\{2\gamma\exp\left(-\frac{1+x^2}{\gamma^2}\right)\right.\\
&\quad\times\left(\exp\left(\frac{2x}{\gamma^2}\right)(2x^2-2x^3+\gamma^2-5x\gamma^2)+\exp\left(\frac{1}{\gamma^2}\right)(-4x^2+2x^3-4\gamma^2+x(2+5\gamma^2))\right)\\
&\quad\left.+\sqrt{\pi}(-8x^3+4x^4-12x\gamma^2+4x^2(1+3\gamma^2)+\gamma^2(2+3\gamma^2))\left(\operatorname{erf}\left(\frac{1-x}{\gamma}\right)+\operatorname{erf}\left(\frac{x}{\gamma}\right)\right)\right\},
\end{aligned}$$

and the initial error can be computed analytically as

$$\begin{aligned}\Pi\Pi[c(\cdot,\cdot)] &= \int_0^1\int_0^1 \exp\left(-\frac{(x-x')^2}{\gamma^2}\right)\frac{x^2(1-x)^2}{B(3,3)}\,\frac{x'^2(1-x')^2}{B(3,3)}\,\mathrm{d}x'\,\mathrm{d}x\\ &= \frac{5}{14}\gamma\left\{-2\gamma\exp\left(-\frac{1}{\gamma^2}\right)\right.\\ &\quad\times\left(-2+7\gamma^2+12\left(-3+7\exp\left(\frac{1}{\gamma^2}\right)\right)\gamma^4+\left(24-72\exp\left(\frac{1}{\gamma^2}\right)\right)\gamma^6\right.\\ &\quad\left.+48\left(-1+\exp\left(\frac{1}{\gamma^2}\right)\right)\gamma^8\right)\\ &\quad\left.+\sqrt{\pi}(4-12\gamma^2+63\gamma^4)\operatorname{erf}\left(\frac{1}{\gamma}\right)\right\}.\end{aligned}$$

## References

1. Fujii Y, Satake K. 2007 Tsunami source of the 2004 Sumatra–Andaman earthquake inferred from tide gauge and satellite data. *Bull. Seismol. Soc. Am.* **97**, S192–S207. (doi:10.1785/0120050613)
2. Synolakis C, Kânoğlu U. 2015 The Fukushima accident was preventable. *Phil. Trans. R. Soc. A* **373**, 20140379. (doi:10.1098/rsta.2014.0379)
3. Satake K, Fujii Y, Harada T, Namegaya Y. 2013 Time and space distribution of coseismic slip of the 2011 Tohoku earthquake as inferred from tsunami waveform data. *Bull. Seismol. Soc. Am.* **103**, 1473–1492. (doi:10.1785/0120120122)
4. Tomita T, Imamura F, Arikawa T, Yasuda T, Kawata Y. 2006 Damage caused by the 2004 Indian Ocean tsunami on the southwestern coast of Sri Lanka. *Coast. Eng. J.* **48**, 99–116. (doi:10.1142/S0578563406001362)
5. Suppasri A, Mas E, Charvet I, Gunasekera R, Imai K, Fukutani Y, Abe Y, Imamura F. 2013 Building damage characteristics based on surveyed data and fragility curves of the 2011 Great East Japan tsunami. *Natural Hazards* **66**, 319–341. (doi:10.1007/s11069-012-0487-8)
6. De Risi R, Goda K, Yasuda T, Mori N. 2017 Is flow velocity important in tsunami empirical fragility modeling? *Earth Sci. Rev.* **166**, 64–82. (doi:10.1016/j.earscirev.2016.12.015)
7. Chock G, Carden L, Robertson I, Olsen M, Yu G. 2013 Tohoku tsunami-induced building failure analysis with implications for US tsunami and seismic design codes. *Earthquake Spectra* **29**, 99–126. (doi:10.1193/1.4000113)
8. Bricker JD, Gibson S, Takagi H, Imamura F. 2015 On the need for larger Manning's roughness coefficients in depth-integrated tsunami inundation models. *Coastal Eng. J.* **57**, 1550005–1. (doi:10.1142/S0578563415500059)
9. Bellos V, Nalbantis I, Tsakiris G. 2018 Friction modeling of flood flow simulations. *J. Hydraulic Eng.* **144**, 04018073. (doi:10.1061/(ASCE)HY.1943-7900.0001540)
10. Kotani M. 1998 Tsunami run-up simulation and damage estimation by using GIS. *P. Coast. Eng., JSCE* **45**, 356–360. (doi:10.2208/proce1989.45.356)
11. Cárdenas G, Catalán PA. 2022 Accelerating tsunami modeling for evacuation studies through modification of the Manning roughness values. *GeoHazards* **3**, 492–507. (doi:10.3390/geohazards3040025)
12. Sraj I, Mandli KT, Knio OM, Dawson CN, Hoteit I. 2014 Uncertainty quantification and inference of Manning's friction coefficients using DART buoy data during the Tōhoku tsunami. *Ocean Model.* **83**, 82–97. (doi:10.1016/j.ocemod.2014.09.001)
13. Siripatana A, Mayo T, Sraj I, Knio O, Dawson C, Le Maitre O, Hoteit I. 2017 Assessing an ensemble Kalman filter inference of Manning'sn coefficient of an idealized tidal inlet against a polynomial chaos-based MCMC. *Ocean Dyn.* **67**, 1067–1094. (doi:10.1007/s10236-017-1074-z)
14. Kaiser G, Scheele L, Kortenhaus A, Løvholt F, Römer H, Leschka S. 2011 The influence of land cover roughness on the results of high resolution tsunami inundation modeling. *Natural Hazards Earth Syst. Sci.* **11**, 2521–2540. (doi:10.5194/nhess-11-2521-2011)
15. Gibbons SJ *et al.* 2022 The sensitivity of tsunami impact to earthquake source parameters and manning friction in high-resolution inundation simulations. *Front. Earth Sci.* **9**, 1–23. (doi:10.3389/feart.2021.757618)

16. Reguly IZ, Giles D, Gopinathan D, Quivy L, Beck JH, Giles MB, Guillas S, Dias F. 2018 The VOLNA-OP2 tsunami code (version 1.5). *Geosci. Model Dev.* **11**, 4621–4635. (doi:10.5194/gmd-11-4621-2018)
17. Giles D, Kashdan E, Salmanidou DM, Guillas S, Dias F. 2020 Performance analysis of Volna-OP2–massively parallel code for tsunami modelling. *Comput. Fluids* **209**, 104649. (doi:10.1016/j.compfluid.2020.104649)
18. Giles D, Gopinathan D, Guillas S, Dias F. 2021 Faster than real time tsunami warning with associated hazard uncertainties. *Front. Earth Sci.* **8**, 597865. (doi:10.3389/feart.2020.597865)
19. Gopinathan D, Heidarzadeh M, Guillas S. 2021 Probabilistic quantification of tsunami current hazard using statistical emulation. *Proc. R. Soc. A* **477**, 20210180. (doi:10.1098/rspa.2021.0180)
20. Salmanidou DM, Beck J, Pazak P, Guillas S. 2021 Probabilistic, high-resolution tsunami predictions in northern Cascadia by exploiting sequential design for efficient emulation. *Natural Hazards Earth Syst. Sci.* **21**, 3789–3807. (doi:10.5194/nhess-21-3789-2021)
21. Li K, Giles D, Karvonen T, Guillas S, Briol FX. 2023 Multilevel Bayesian quadrature. In *The 26th Int. Conf. on Artificial Intelligence and Statistics*, 25–27 April 2023, pp. 1845–1868. Valencia, Spain: PMLR.
22. Fukutani Y, Yasuda T, Yamanaka R. 2023 Efficient probabilistic prediction of tsunami inundation considering random tsunami sources and the failure probability of seawalls. *Stoch. Environ. Res. Risk Assess.* **37**, 1–16. (doi:10.1007/s00477-023-02379-3)
23. Ehara A, Guillas S. 2023 An adaptive strategy for sequential designs of multilevel computer experiments. *Int. J. Uncertain. Quantification* **13**, 61–98. (doi:10.1615/Int.J.UncertaintyQuantification.2023038376)
24. Ehara A, Salmanidou DM, Heidarzadeh M, Guillas S. 2023 Multi-level emulation of tsunami simulations over Cilacap, South Java, Indonesia. *Comput. Geosci.* **27**, 127–142. (doi:10.1007/s10596-022-10183-1)
25. Pranantyo IR, Heidarzadeh M, Cummins PR. 2021 Complex tsunami Hazards in Eastern Indonesia from seismic and non-seismic sources: deterministic modelling based on historical and modern data. *Geosci. Lett.* **8**, 20. (doi:10.1186/s40562-021-00190-y)
26. Okada Y. 1985 Surface deformation due to shear and tensile faults in a half-space. *Bull. Seismol. Soc. Am.* **75**, 1135–1154. (doi:10.1785/BSSA0750041135)
27. Lay T *et al.* 2005 The great Sumatra-Andaman earthquake of 26 december 2004. *Science* **308**, 1127–1133. (doi:10.1126/science.1112250)
28. Heidarzadeh M, Harada T, Satake K, Ishibe T, Takagawa T. 2017 Tsunamis from strike-slip earthquakes in the Wharton Basin, northeast Indian Ocean: March 2016 M w7. 8 event and its relationship with the April 2012 M w 8.6 event. *Geophys. J. Int.* **211**, 1601–1612. (doi:10.1093/gji/ggx395)
29. Hayes GP, Moore GL, Portner DE, Hearne M, Flamme H, Furtney M, Smoczyk GM. 2018 Slab2, a comprehensive subduction zone geometry model. *Science* **362**, 58–61. (doi:10.1126/science.aat4723)
30. GEBCO Compilation Group (2022). 2022. The GEBCO_2022 Grid – a continuous terrain model of the global oceans and land. (doi:10.5285/e0f0bb80-ab44-2739-e053-6c86abc0289c).
31. Roberts KJ, Pringle WJ, Westerink JJ. 2019 OceanMesh2D 1.0: MATLAB-based software for two-dimensional unstructured mesh generation in coastal ocean modeling. *Geosci. Model Dev.* **12**, 1847–1868. (doi:10.5194/gmd-12-1847-2019)
32. Yeh H. 2006 Maximum fluid forces in the tsunami runup zone. *J. Waterway, Port, Coastal, Ocean Eng.* **132**, 496–500. (doi:10.1061/(ASCE)0733-950X(2006)132:6(496))
33. Park H, Cox DT, Lynett PJ, Wiebe DM, Shin S. 2013 Tsunami inundation modeling in constructed environments: a physical and numerical comparison of free-surface elevation, velocity, and momentum flux. *Coastal Eng.* **79**, 9–21. (doi:10.1016/j.coastaleng.2013.04.002)
34. Attary N, van de Lindt JW, Unnikrishnan VU, Barbosa AR, Cox DT. 2017 Methodology for development of physics-based tsunami fragilities. *J. Struct. Eng.* **143**, 04016223. (doi:10.1061/(ASCE)ST.1943-541X.0001715)
35. Gayer G, Leschka S, Nöhren I, Larsen O, Günther H. 2010 Tsunami inundation modelling based on detailed roughness maps of densely populated areas. *Natural Hazards Earth Syst. Sci.* **10**, 1679–1687. (doi:10.5194/nhess-10-1679-2010)
36. Diaconis P. 1988 Bayesian numerical analysis. *Stat. Deci. Theory Related Topics IV* **1**, 163–175. (doi:10.1007/978-1-4613-8768-8_20)
37. O'Hagan A. 1991 Bayes–hermite quadrature. *J. Stat. Plann. Inference* **29**, 245–260. (doi:10.1016/0378-3758(91)90002-V)

38. Rasmussen CE, Ghahramani Z. 2003 Bayesian Monte carlo. In *Advances in Neural Information Processing Systems* (eds S Becker, S Thrun, K Obermayer), pp. 505–512. MIT Press.
39. Park H, Cox DT, Barbosa AR. 2017 Comparison of inundation depth and momentum flux based fragilities for probabilistic tsunami damage assessment and uncertainty analysis. *Coastal Eng.* **122**, 10–26. (doi:10.1016/j.coastaleng.2017.01.008)
40. Salmanidou DM, Ehara A, Himaz R, Heidarzadeh M, Guillas S. 2021 Impact of future tsunamis from the Java trench on household welfare: merging geophysics and economics through catastrophe modelling. *Int. J. Disaster Risk Reduct.* **61**, 102291. (doi:10.1016/j.ijdrr.2021.102291)
41. Iglesias O, Lastras G, Souto C, Costa S, Canals M. 2014 Effects of coastal submarine canyons on tsunami propagation and impact. *Mar. Geol.* **350**, 39–51. (doi:10.1016/j.margeo.2014.01.013)
42. Liu X, Guillas S. 2017 Dimension reduction for Gaussian process emulation: an application to the influence of bathymetry on tsunami heights. *SIAM/ASA J. Uncert. Quant.* **5**, 787–812. (doi:10.1137/16M1090648)
43. Kaiyu L, Serge G. 2025 Uncertainty in Manning's roughness coefficient in multilevel simulations of future tsunamis in Sumatra. Github. (https://github.com/CeciliaKaiyu/UQfriction)
44. Kaiyu L, Serge G. 2025 Uncertainty in Manning's roughness coefficient in multilevel simulations of future tsunamis in Sumatra. Zenodo. (doi:10.5281/zenodo.15015626)
45. Wessel P, Luis J, Uieda L, Scharroo R, Wobbe F, Smith WH, Tian D. 2019 The generic mapping tools version 6. *Geochem. Geophys. Geosyst.* **20**, 5556–5564. (doi:10.1029/2019GC008515)